scientific reports

OPEN

Tailoring plasmon excitations in $\alpha - \mathcal{T}_3$ armchair nanoribbons

Andrii Iurov[1✉], Liubov Zhemchuzhna[1,2], Godfrey Gumbs[2,3], Danhong Huang[4,5], Paula Fekete[6], Farhana Anwar[7], Dipendra Dahal[8] & Nicholas Weekes[1,9]

We have calculated and investigated the electronic states, dynamical polarization function and the plasmon excitations for $\alpha - \mathcal{T}_3$ nanoribbons with armchair-edge termination. The obtained plasmon dispersions are found to depend significantly on the number of atomic rows across the ribbon and the energy gap which is also determined by the nanoribbon geometry. The bandgap appears to have the strongest effect on both the plasmon dispersions and their Landau damping. We have determined the conditions when relative hopping parameter α of an $\alpha - \mathcal{T}_3$ lattice has a strong effect on the plasmons which makes our material distinguished from graphene nanoribbons. Our results for the electronic and collective properties of $\alpha - \mathcal{T}_3$ nanoribbons are expected to find numerous applications in the development of the next-generation electronic, nano-optical and plasmonic devices.

Graphene nanoribbons (GNRs) are now one of the most intensively investigated two-dimensional (2D) materials in the field of low-dimensional nanoelectronic devices. This is due to their sensitive dependence on the width and nature of their the edges of the nanoribbons. They also display a number of fundamental physical and technologically promising properties, as well as some unique and unprecedented physical phenomena in comparison with corresponding bulk materials[1]. These includes exotic and non-trivial topological electronic states (Majorana fermions)[2,3], spin-momentum locked and correlated transport channels, and arrays of plasmonic nano-antennas[4]. In addition, specific electronic quantum phases could be created at junctions of armchair nanoribbons[5]. Transport of charge carriers was studied in networks of armchair nanoribbons, and the possibility for creating a reproducible field-effect transistor with much higher carrier mobility was also demonstrated[6]. Furthermore, plasmonics is playing a major role in designing low-dimensional optical devices since the localized field induced by collective excitations could be closely confined within a nano-size ribbon, resulting in a distinct plasmon mode accompanied by a huge enhancement in the surrounding optical field[7–10]. Specific types of plasmon excitation in nanoribbons[11] acquire some important and sometimes unexpected features and applications in sensing and nano-imaging[12–14]. Similarly, the plasmons were extensively studies in graphene[15,16] and other bulk Dirac materials. After more than a decade of uninterrupted efforts[17–24], many-body theory on low-dimensional materials has finally been developed and becomes a huge resource for in-depth exploration of plasmon dynamical properties. This success is mainly attributed to accurately calculating the dynamical polarization function[25], which is also related to the effect of static screening on transport properties of electrons.

From a physical point of view, we expect all nanoribbon electronic properties will depend strongly on their width and type of termination[26,27] as well zigzag[28,29] and armchair[30–32]. In practice, the studies of quantum size-effect and nonlocality of plasmons, dielectric and optical responses in both nanoribbons[33], and nanodisks have already revealed a substantial plasmon broadening, much larger for zigzag in comparison with the armchair case[34]. Meanwhile, a tunable bandgap, which is not present for graphene but could be produced by applying an optical field[35–37], is desirable for most semiconductor devices and depends on the width of armchair nanoribbon[27,32,38]. Consequently, such a bandgap could be adjusted by employing armchair GNRs with various numbers of atomic cells across a ribbon.

[1]Department of Physics and Computer Science, Medgar Evers College of the City University of New York, Brooklyn, NY 11225, USA. [2]Department of Physics and Astronomy, Hunter College of the City University of New York, 695 Park Avenue, New York, NY 10065, USA. [3]Donostia International Physics Center (DIPC), P de Manuel Lardizabal, 4, 20018 San Sebastian, Basque Country, Spain. [4]Air Force Research Laboratory, Space Vehicles Directorate, Kirtland Air Force Base, Albuquerque, NM 87117, USA. [5]Center for High Technology Materials, University of New Mexico, 1313 Goddard SE, Albuquerque, NM 87106, USA. [6]US Military Academy at West Point, 606 Thayer Road, West Point, NY 10996, USA. [7]Lawrence Berkeley National Laboratory, 1 Cyclotron Road, Berkeley, CA 94720, USA. [8]Texas Center for Superconductivity and Department of Physics, University of Houston, Houston, TX 77204, USA. [9]Department of Information Systems and Cybersecurity, Grove School of Engineering, The City College of New York, 275 Convent Avenue, New York, NY 10031, USA. ✉email: aiurov@mec.cuny.edu

Electronic and collective properties of a GNR could be used for high-frequency electronics, nano-scale circuit fabrication and production, of various kinds of very-long-wavelength sensing, and ultrafast electric and light modulations[39]. While low-loss graphene is technologically regarded as a promising replacement for high-frequency plasmonic materials like metals, nanoribbons have become especially attractive since a very strong, induced electric field resulting from resonant plasmons can be sustained across a narrow spatially-confined channel, and furthermore, this resulting electric field could be modified by patterned electrostatic gating[40–42].

It is important to point out that efficient, reliable and affordable techniques for fabrication of nanoribbons with a given width have already become accessible through chemical vapor deposition[43–45], in addition to earlier atomically-precise bottom-up fabrication[46] using chemically or lithographically unzipping a carbon nanotube[47].

From another perspective, among all newly emergent and recently discovered 2D nanostructures[48,49], the $\alpha - \mathcal{T}_3$ model represents one of the most unusual and promising materials. Its atomic structure consists of a hexagonal-honeycomb lattice as in graphene plus an atom located at the center of each hexagon, i.e. a hub (or H) atom. The interaction strength, resulting from electron hopping integral between H and either remaining A or B rim atom, differs from that between nearest-neighbor rim atoms of the hexagon. In this case, the relative hopping parameter $\alpha = t_{\text{hub-rim}}/t_{\text{rim-rim}}$ varies only between 0 and 1, where $\alpha = 0$ corresponds to graphene with a completely detached set of hub atoms, whereas $\alpha = 1$ refers to the dice lattice. Therefore, such an $\alpha - \mathcal{T}_3$ model is regarded as an interpolation between graphene and a dice lattice. In reality, a number of $\alpha - \mathcal{T}_3$ materials have already been fabricated successfully[50]. The $\alpha - \mathcal{T}_3$ lattice structure leads to a pseudospin-1 Dirac-Weyl Hamiltonian, and the resulting metallic (gapless) low-energy band structure involves a Dirac cone as well as an additional dispersionless flat band. This flat band makes the $\alpha - \mathcal{T}_3$ topologically distinguished from any other Dirac materials and appears very to be stable and robust against the presence of external fields[51–53], or a disorder. Another noticeable effects of this flat band appears as a reduced electron mobility in $\alpha - \mathcal{T}_3$ material due to the zero group velocity $\simeq d\varepsilon(\mathbf{k}_\parallel)/dk_i$ associated with this flat band for $i = 1$, 2, as well as new physics features for plasmon excitations and their Landau damping[22].

A bandgap could also be generated in a dice lattice[54,55], similar to the situation for graphene. Recently, Dirac semimetals also showed some interesting electronic properties[56,57], although they closely resemble but not completely the same as those of $\alpha - \mathcal{T}_3$. As a matter of fact, the unique electronic band structure of the $\alpha - \mathcal{T}_3$ model has proven to be responsible for its unusual electronic, optical, collective, magnetic and topological properties[58–77] which have been investigated extensively over the last several years.

In spite of the fact that $\alpha - \mathcal{T}_3$ materials were only discovered recently, there has just been a handful of crucial publications on the subject of nanoribbons made from such materials. Group velocities and current distributions in these ribbons were studied in Ref.[78] with both armchair and zigzag terminations in the presence of a magnetic field. Importantly, a comprehensive investigation on dice lattice with $\alpha = 1$ indicated a difference in electronic states compared to zigzag graphene nanoribbons[79]. Moreover, electronic states under a magnetic field were calculated in Ref.[80] for both armchair and zigzag configurations. Meanwhile, mean-field computations on effects due to strain[81] hsvr revealed a phase transition from antiferromagnetic to ferromagnetic behavior with increasing α value in analogy with the paramagnetic transition in bulk $\alpha - \mathcal{T}_3$[82,83], and this ferromagnetic ordering in dice ribbons was further explored in Ref.[84]. For $\alpha - \mathcal{T}_3$ materials, a valley dependence in both bulk[51] and nanoribbons[85] is of the highest interest. Most previous theoretical papers on GNR plasmonics deal with a particular case having semi-metallic gapless energy bands and low-level electron doping, for which an approximate analytic calculation for plasmon dispersion could be performed in the long wavelength limit[26,86,87]. Although such simplified approaches are considered realistic and important, they are very limited because both the Dirac Hamiltonian and $\mathbf{k} \cdot \mathbf{p}$ model only work well for wide nanoribbons in which several subbands are populated even for moderate doping levels. However, an important case with a finite bandgap has seldomly received enough attention even for earlier studies on graphene nanoribbons. In view of this, the primary focus of our paper is on studying the dependence of plasmon dispersion and their damping on nanoribbon width, which determines the splitting gap between energy subbands, electron doping density, and especially on the relative hopping parameter α.

Phase-dependent electronic states in nanoribbons

Our starting point here is a calculation of both the wave functions and low-energy dispersion of electrons in an $\alpha - \mathcal{T}_3$ nanoribbon associated with a bulk pseudospin-1 Dirac-Weyl Hamiltonian[22]

$$\mathbb{H}_b^{\tau,\phi}(\mathbf{k}) = \gamma_0 \left\{ \begin{matrix} 0 & k_-^\tau \cos\phi & 0 \\ k_+^\tau \cos\phi & 0 & k_-^\tau \sin\phi \\ 0 & k_+^\tau \sin\phi & 0 \end{matrix} \right\}. \tag{1}$$

In this notation, $\gamma_0 = \hbar v_F/\sqrt{2}$, $k_\pm^\tau = \tau k_x \pm i k_y$ depends on the valley index τ for two non-equivalent K and K' valleys. We emphasize that we confine our attention to low-energy states of electrons near these valleys with separation $\delta K_x = K - K' = 4\pi/\sqrt{3}\, a_0$ and $\delta K_y = 0$ where a_0 is the lattice constant, as presented in Fig. 1d. For this, the relative hopping parameter α is related to the geometrical phase ϕ in Eq. (1) (also called Berry phase sometimes although the real Berry phase is $\pm\pi\cos(2\phi)$ for the conical bands and $\mp 2\pi\cos(2\phi)$ for the flat band of $\alpha - \mathcal{T}_3$)[51,88] by $\alpha = \tan\phi$. As shown in Fig. 1a and b, $a_0 = 0.142$nm represents the lattice constant (bond length between two nearest identical atoms, e.g., B-to-B) and $a = a_0/\sqrt{3}$ is the side length of a hexagon.

In bulk $\alpha - \mathcal{T}_3$, solutions for three low-energy bands are $\varepsilon_{\tau,\phi}^\sigma(\mathbf{k}) = \sigma\, \hbar v_F k$ with $\sigma = \pm 1$ labeling the valence $(-)$ and conduction $(+)$ bands, respectively, and they are identical to those of graphene. Apart from these two subbands, the Hamiltonian in Eq. (1) yields an additional solution $\varepsilon_{\tau,\phi}^{\sigma=0}(\mathbf{k}) \equiv 0$ which represents a dispersionless or flat band. Such general schematics with a lower valence, an upper conduction and a middle flat band are retained for nanoribbons. We also note that all these energy dispersions do not depend on the valley index τ in contrast to the phases contained in corresponding wave functions.
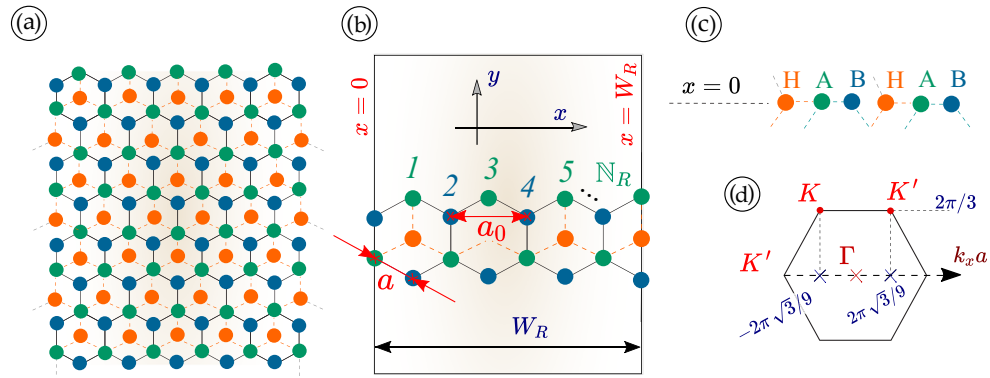
Figure 1. Schematic illustrations for three sublattices (A, B, H) of $\alpha - \mathcal{T}_3$ armchair nanoribbons. Panels (**a**) and (**b**) depict representations of a nanoribbon with armchair termination for defining the width W_R of a nanoribbon with inter-atom distance a and lattice constant a_0. Panel (**c**) demonstrates the edge-row configurations and transverse boundary conditions along the x axis for an armchair edge of $\alpha - \mathcal{T}_3$ or a dice lattice, where the letters H, A, B label hub and hexagonal-rim atoms of two sublattices. Panel (**d**) illustrates the first Brillouin zone and the wave vectors K and K' of two valleys.

Chosen finite width and edge termination of a ribbon determine its electronic properties. These include the quantization of electron transverse momentum and the presence of splitting gaps between different electron subbands. The width W_R of a ribbon determines the number of atomic rows $\mathbb{N}_R$ across the ribbon through $W_R = (a_0/2)(\mathbb{N}_R + 1) = \sqrt{3}a(\mathbb{N}_R + 1)/2$ as shown in Fig. 1a through Fig. 1c. Here, $\mathbb{N}_R$ is the total number of atomic rows including all types (A, B and H) of lattice atoms but *excluding the two boundary rows where the wave function would vanish*. The width of the ribbon shown in Fig. 1b is obviously $3.5\mathbb{N}_R$.

The boundary conditions for the wave function are the same as those for a dice lattice[79] by requiring that all three sublattice probability currents, including one for H atom, disappear at each boundary of a nanoribbon. This gives rise to $\varphi_\nu(x)\big|_{x=0} = \varphi'_\nu(x)\big|_{x=0}$ and $\varphi_\nu(x)\big|_{x=W_R} = \exp(i\delta K_x W_R)\,\varphi'_\nu(x)\big|_{x=W_R}$, where $\nu = A$, B and H, $\varphi_\nu(x)$ and $\varphi'_\nu(x)$ correspond to wave function components belonging to K and K' valleys, respectively. From the armchair boundary conditions, it is clear that the boundary conditions have mixed the electronic states from both K and K' valleys, similar to graphene[26], and therefore both valleys need to be considered.

The energy dispersions for an $\alpha - \mathcal{T}_3$ armchair nanoribbon obtained in Sect. I of the Supplementary Information appear to be the same for previously considered limiting cases of graphene (except for the presence of the flat band) and a dice lattice: $\varepsilon_n^\sigma(k_y) = \sigma\gamma_0\sqrt{k_y^2 + \xi_n^2}$ with $\sigma = 0, \pm 1$. The dispersion relations look similar to bulk $\alpha - \mathcal{T}_3$ but with quantized transverse momentum obtained from the condition

$$2\xi_n W_R = 2\pi n + \delta K_x W_R, \quad n = 0, \pm 1, \pm 2, \pm 3, \cdots, \tag{2}$$

which determines the quantized transverse wave number ξ_n and energy subbands. These agree with previous results for graphene[26,89] ($\alpha = 0$) and a dice lattice[79] ($\alpha = 1$). The α-independent result in Eq. (2) tells us that the subband-energy dispersions $\varepsilon_n(k_y)$ will be the same for both graphene and $\alpha - \mathcal{T}_3$ materials except for an additional flat band in the middle, which is similar to the case of two bulk materials. Explicitly, from Eq. (2) we obtain the quantized transverse wave number ξ_n of electrons, given by

$$\xi_n = \frac{\pi n}{W_R} - \frac{2\pi}{3a_0} = \frac{2\pi}{\sqrt{3}\,a}\left(\frac{n}{\mathbb{N}_R + 1} - \frac{1}{3}\right) = \frac{2\pi}{3\sqrt{3}\,a}\frac{3n - \mathbb{N}_R - 1}{\mathbb{N}_R + 1}. \tag{3}$$

The obtained dispersions imply that the $n = 1$ energy subband may not be the lowest one in contrast to the case for a quantum well. As expected, some of the calculated low-energy subbands $\varepsilon_N^\sigma(k_y)$ presented in Fig. 2a–c do depend on the quantum number n and the number of row atoms $\mathbb{N}_R$. Interestingly, the bandgap between the lowest conduction subband and the highest valence subband varies with W_R or $\mathbb{N}_R$, becoming finite for $\mathbb{N}_R = 49$ and 51 but zero for $\mathbb{N}_R = 50$.

As a matter of fact, the energy gap between the first valence (or conduction) subband and the middle flat band at zero energy, i.e., half of the bandgap, is found to be

$$\Delta_0(\mathbb{N}_R) = \frac{2\pi}{3a_0}\left(\frac{\gamma_0}{\mathbb{N}_R + 1}\right)\min_{n\in\{N_\Delta\}}(3n - \mathbb{N}_R - 1), \tag{4}$$

where the minimal value of $3n - \mathbb{N}_R - 1$ for a given ribbon width $\mathbb{N}_R$ is assumed to be achieved for integer numbers n_Δ, and $\Delta_0(\mathbb{N}_R)$ becomes zero if $\mathbb{N}_R + 1$ becomes divisible by 3. Therefore, $N_0 = (\mathbb{N}_R + 1)/3$ enables specifying the lowest pair of metallic subbands which touch each other, and the flat band as well, at the Dirac point. Otherwise, n_Δ should be the smaller one of following two numbers, i.e., $n_\Delta^\pm = \text{InP}[(\mathbb{N}_R + 1)/3] \pm 1$, where InP($x$) is a function by taking the integer part of a rational number x. The calculated $\Delta_0(\mathbb{N}_R)$ as a function of $\mathbb{N}_R$ is presented in Fig. 2d, from which we find $\Delta_0(\mathbb{N}_R)$ does go to zero for a set of selected values of $\mathbb{N}_R$ or W_R. All the other (higher) subband dispersions are doubly degenerate, as seen in Fig. 2a–c. Meanwhile, we also find
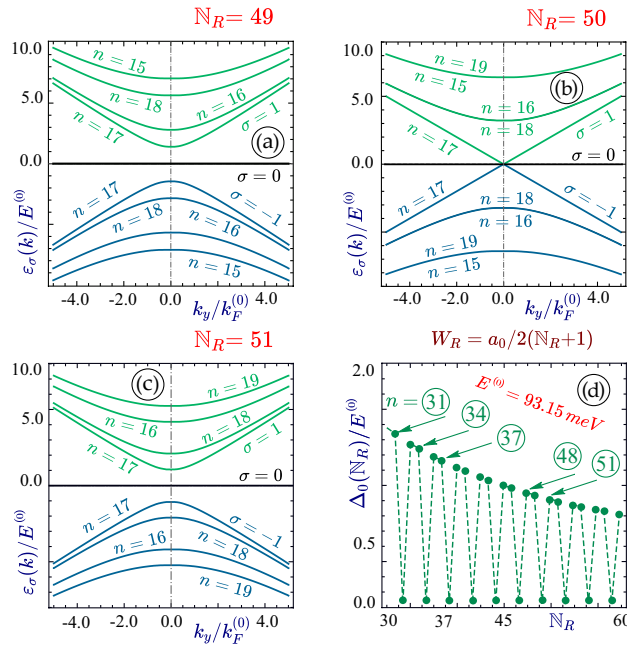
Figure 2. Calculated low-energy subbands $\varepsilon_n^\sigma(k_y)$ of $\alpha - \mathcal{T}_3$ armchair nanoribbons with different widths W_R. Panels (**a**) through (**c**) present dispersion relations of some low-energy subbands as functions of the longitudinal wave vector k_y for ribbons with $\mathbb{N}_R = 49, 50, 51$ atomic rows, respectively. Panel (**d**) shows the calculated half-bandgap $\Delta_0(\mathbb{N}_R)$ of nanoribbons between the lowest conduction and the middle flat subband for various selected $\mathbb{N}_R$ values. In our computations, we set units as $k_F^{(0)} = (\pi/2)(10^8 \mathrm{m}^{-1}) = 1.57 \times 10^8 \mathrm{m}^{-1}$, $L_0 = 1/k_F^{(0)} = 6.33\mathrm{nm}$, $E^{(0)} = \gamma_0 k_F^{(0)} = 93.15\mathrm{meV}$ and $\Omega_0 = 1.42 \times 10^{14}\mathrm{Hz}$.

that both subband separation and energy gap are greatly enhanced for a narrower ribbon, similar to the case for a quantum well, which makes it difficult to occupy more than one subband for a range of experimentally-accessible doping levels.

The wave function for an armchair nanoribbon takes the form

$$\Phi_\sigma^\phi(n \,|\, x, k_y) = \left\{ \begin{array}{c} \Psi_\sigma^{\mathbf{K}, \phi}(n \,|\, x, k_y) \\ \Psi_\sigma^{\mathbf{K}', \phi}(n \,|\, x, k_y) \end{array} \right\}. \tag{5}$$

Each of the two components in Eq. (5) is related to a specific valley ($\tau = \pm 1$) and formally written as

$$\Psi_{\sigma=\pm1}^{\tau, \phi}(n \,|\, x, k_y) = \frac{1}{\sqrt{\mathcal{L}_0 W_R}} \, \varphi_{\sigma=\pm1}^{\tau, \phi}(n \,|\, x) \, \mathrm{e}^{ik_y y}, \tag{6}$$

where $\mathcal{L}_0$ is the ribbon length,

$$\varphi_{\sigma=\pm1}^{\tau, \phi}(n \,|\, x) = \frac{1}{\sqrt{2}} \begin{bmatrix} \tau \cos\phi \, \mathrm{e}^{-i\tau\Theta_n(k_y)} \\ \sigma \\ \tau \sin\phi \, \mathrm{e}^{i\tau\Theta_n(k_y)} \end{bmatrix} \exp(i\tau\xi_n x). \tag{7}$$

and $\Theta_n(k_y) = \tan^{-1}(k_y/\xi_n)$. It is crucial to notice that only the electron/hole index $\sigma = \pm 1$, not the subband index n, determines the $\pm$ sign of energy dispersions $\varepsilon_n^\sigma(k_y)$.

The eigenvalue equation in $\alpha - \mathcal{T}_3$ allows for an additional zero-energy solution with for a flat band ($\sigma = 0$) which is

$$\Psi_{\sigma=0}^{\tau, \phi}(n \,|\, x, k_y) = \frac{1}{\sqrt{\mathcal{L}_0 W_R}} \, \varphi_{\sigma=0}^{\tau, \phi}(n \,|\, x) \, \mathrm{e}^{ik_y y}, \tag{8}$$

where

$$\varphi_{\sigma=0}^{\tau, \phi}(n \,|\, x) = \begin{bmatrix} (\tau\zeta_n - ik_y)\sin\phi \\ 0 \\ -(\tau\zeta_n + ik_y)\cos\phi \end{bmatrix} \frac{\mathrm{e}^{i\tau\zeta_n x}}{\sqrt{\zeta_n^2 + k_y^2}} = \begin{bmatrix} \tau\sin\phi \, \mathrm{e}^{-i\tau\Theta_n(k_y)} \\ 0 \\ -\tau\cos\phi \, \mathrm{e}^{i\tau\Theta_n(k_y)} \end{bmatrix} \exp(i\tau\xi_n x), \tag{9}$$

in which $\mathbf{K}$ and $\mathbf{K}'$ valleys correspond to $\tau = \pm 1$ and $\Theta_n(k_y) = \tan^{-1}(k_y/\zeta_n)$ and $\zeta_n = |\xi_n|$ given by Eq. (3).

As far as the obtained electronic states are concerned, we would like to emphasize that the type, structure and dependence of the wave functions in Eqs. (7) and (9) are very similar in nature to those for the bulk material.

However, the transverse wave vector ξ_n and the quantum phase $\Theta_n(k_y)$, are now fully quantized (or discrete), and the quantization conditions in Eq. (3) are identical and include the mixing of K and K' valleys.

Polarization function, plasmon dispersions and damping

For an ideal graphene nanoribbon without edge defects, by using standard many-body theory, the dielectric-function tensor within the random-phase approximation (RPA) can be generally expressed as

$$\epsilon_{\mu,\nu}^{\lambda,\rho}(q_y,\omega\,|\,E_F,\alpha) = \delta_{\lambda,\mu}\,\delta_{\rho,\nu} - V_{\mu,\nu}^{\lambda,\rho}(q_y)\,\Pi_{\mu,\nu}^{(0)}(q_y,\omega\,|\,E_F,\alpha)\,, \tag{10}$$

where E_F denotes the Fermi energy of the system, q_y is the longitudinal transfer wave vector along a nanoribbon and ω is the angular frequency of a perturbing field. Here, each of the indices λ,ρ,μ,ν is a composite one which includes the subband index i and band index σ for the conduction, valence and flat bands, i.e., $\lambda = \{i,\sigma\}$. The plasmon modes of the structure can be computed from the zero determinant of the dielectric-function tensor in Eq. (10), leading to

$$\mathcal{D}et\left[\epsilon_{\mu,\nu}^{\lambda,\rho}(q_y,\omega\,|\,E_F,\alpha)\right] = \mathcal{D}et\left[\delta_{\lambda,\mu}\delta_{\rho,\nu} - V_{\mu,\nu}^{\lambda,\rho}(q_y)\,\Pi_{\mu,\nu}^{(0)}(q_y,\omega\,|\,E_F,\alpha)\right] = 0\,. \tag{11}$$

The diagonal matrix elements in Eq. (10) are connected to dispersions of individual plasmon modes, while the off-diagonal matrix elements describe the couplings between different plasmon modes.

Within the RPA, the introduced subband polarization function $\Pi_{\mu,\nu}^{(0)}(q_y,\omega)$ in Eq. (10) is calculated as

$$\Pi_{\mu,\nu}^{(0)}(q_y,\omega\,|\,E_F,\alpha) = \frac{g_s}{2\pi}\int\limits_{1^{st}\,BZ} dk_y\left\{\frac{f_0[\varepsilon_\mu(k_y)] - f_0[\varepsilon_\nu(k_y+q_y)]}{\hbar(\omega+i\delta) + \varepsilon_\mu(k_y) - \varepsilon_\nu(k_y+q_y)}\right\}\mathbb{O}_{\sigma_\mu\leftrightarrow\sigma_\nu}^{m,n}(k_y,q_y\,|\,\alpha)\,, \tag{12}$$

where the integral with respect to wave vector k_y is limited to the first Brillouin zone, $g_s = 2$ takes into account the spin degeneracy, $\delta \ll \omega$ represents a homogeneous diagonal-dephasing rate of electrons and $\varepsilon_\mu(k_y)$ is the subband energy, $f_0(x)$ is the Fermi-Dirac distribution function for thermal-equilibrium electrons at temperature T and chemical potential $u_0(T)$. At $T = 0$,

$$f_0[\varepsilon_\mu(k_y)\,|\,u_0(T), T\to 0] = \left\{1 + \exp\left[\frac{\varepsilon_\mu(k_y) - u_0(T)}{k_B T}\right]\right\}^{-1}\Bigg|_{T\to 0} \to \delta_{\sigma,-1} + \delta_{\sigma,0} + \delta_{\sigma,1}\,\Theta[E_F - \varepsilon_m(k_y)]\,, \tag{13}$$

where E_F is the Fermi energy and $\Theta(x)$ is a Heaviside step function.

Next, since the mirror symmetry between conduction and valence subbands is retained in our system, as it is for graphene nanoribbons, it guarantees that the orbital part of the wave function will not depend on band selection. Consequently, such a unique property greatly simplifies the Coulomb interaction $V_{\mu,\nu}^{\lambda,\rho}(q_y)$ employed in Eq. (10), leading to

$$V_{j',m'}^{j,m}(q_y) = \frac{e^2}{2\pi\epsilon_0\epsilon_b}\int\limits_0^1 du\int\limits_0^1 du'\,\cos[\pi(j-m)u]\,\cos[\pi(j'-m')u']\,K_0(|q_y|W_R|u-u'|) \equiv V_{j'-m'}^{j-m}(q_y)\,, \tag{14}$$

which is significant only for $j - j' = 0$ and $m - m' = 0$, as demonstrated in Fig. 3a. Moreover, the Coulomb interaction in Eq. (14) is also independent of the phase ϕ, and therefore, remains the same for all $\alpha - \mathcal{T}_3$ materials including graphene[89]. In the long-wavelength limit $q_y \to 0$, the Bessel function $K_0(x)$ of the second kind diverges as $-\log(x)$, corresponding to $\simeq 1/\sqrt{q_x^2 + q_y^2}$ behavior for the 2D case. In this case, the Coulomb-interaction matrix elements connect two initial and two final states with the same band and subband indices, leading to one for intra-subband excitation only, i.e.

$$\epsilon_{\mu,\nu}(q_y,\omega\,|\,E_F,\alpha) \equiv \epsilon_{\mu,\nu}^{\mu,\nu}(q_y,\omega\,|\,E_F,\alpha) \approx \delta_{\sigma_\mu,\sigma_\nu}\delta_{m,n} - V_0^0(q_y)\,\Pi_{\nu,\nu}^{(0)}(q_y,\omega\,|\,E_F,\alpha)\,, \tag{15}$$

which is a regular 2D matrix ($3N \times 3N$), where $\nu = \{n,\sigma_\nu\}$ and N is the total number of subbands taken into consideration.

Finally, the determinant $\mathcal{D}et$ and the trace $\mathcal{T}r$ of the matrix in Eq. (15) are (see Sect. II of our Supplementary Information) connected by

$$\mathcal{D}et\left[\epsilon_{\mu\nu}(q_y,\omega)\right] = 1 - V_0^0(q_y)\sum_\nu \Pi_{\nu,\nu}^{(0)}(q_y,\omega\,|\,E_F,\alpha) = \mathcal{T}r\left[\epsilon_{\mu\nu}(q_y,\omega)\right] - 3N + 1\,, \tag{16}$$

which was also employed in Ref.[89] for graphene. In our calculation, the actual polarization function is obtained as the sum of ten lowest subbands around n_0.

As a last step, we turn to calculate the wave-function overlaps (or prefactors) $\mathbb{O}_{\pm 1,0\leftrightarrow\pm 1,0}^{n,n'}(k_y,q_y)$ introduced in Eq. (12) for the polarization function. For $\alpha - \mathcal{T}_3$ nanoribbons, it is explicitly defined by $\mathbb{O}_{\pm 1,0\leftrightarrow\pm 1,0}^{n,n'}(k_y,q_y) \equiv \left|\langle\Phi_\sigma^\phi(n\,|\,x,k_y)\,|e^{iq_x x}|\,\Phi_\sigma^\phi(n'\,|\,x,k_y+q_y)\rangle\right|^2$ where $\sigma = 0,\pm 1$ and the complete wave functions $\Phi_\sigma^\phi(n\,|\,x,k_y)$ and $\Phi_\sigma^\phi(n'\,|\,x,k_y+q)$ have already been given by Eq. (5).
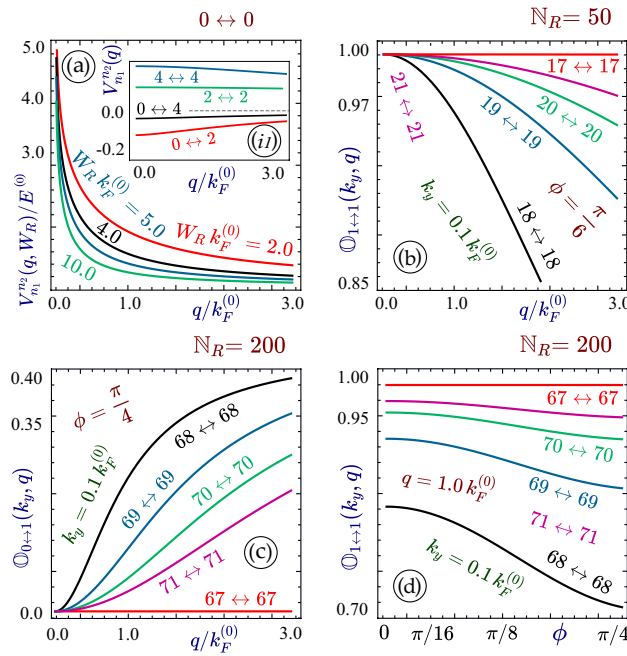
Figure 3. Panel (**a**) shows the Coulomb potential $V_{n_1}^{n_2}(|q_y|W_R)$ with $n_1 = i - j = 0$ and $n_2 = m - n = 0$ as a function of the transfer wave vector q_y for chosen widths W_R, and its inset (*i1*) displays the remaining potential elements with nonzero n_1 or n_2, as labeled. Panels (**b**) through (**d**) present *intra-subband* ($n_1 = n_2$) overlaps $\mathbb{O}_{\sigma_1 \leftrightarrow \sigma_2}^{n_1,n_1}(k_y, q_y)$ for various types of *intra* ($0 \leftrightarrow 1$) and *inter-band* ($1 \leftrightarrow 1$) transitions as functions of q_y in (**b**), (**c**) and phase ϕ in (**d**). Here, $\mathbb{N}_R$ is set as 50, 50, 200 in (**b**), (**d**). Other parameters are the same as those in Fig. 2.

Using earlier wavefunctions (5), we get $\mathbb{O}_{\pm 1 \leftrightarrow 1}^{n,n'}(k_y, q_y) = \frac{1}{4}\left[1 \pm \cos[\Theta_{n,n'}(k_y, q_y)]\right]^2 + \frac{1}{4}\cos^2(2\phi)\sin^2[\Theta_{n,n'}(k_y, q_y)]$ and $\mathbb{O}_{0 \leftrightarrow 1}^{n,n'}(k_y, q_y) = \frac{1}{2}\sin^2(2\phi)\sin^2[\Theta_{n,n'}(k_y, q_y)]$ which are the same as our obtained result for bulk $\alpha - \mathcal{T}_3$[90] since $\mathbb{O}_{\pm 1,0 \leftrightarrow \pm 1,0}^{n,n'}(k_y, q_y)$ does not depend on the valley index τ while the wave function in Eq. (5) for an armchair nanoribbon is just a combination of states from these two valleys. Therefore, the overlap can be regarded as an average between two inequivalent valleys. On the other hand, the wave functions in Eq. (5) do depend on the band indices so that the results are different, corresponding to various types of transitions (i.e., from and to valence, flat, and conduction bands). For graphene with $\alpha = 1$, we easily verify that $\mathbb{O}_{\pm 1 \leftrightarrow 1}^{n,n'}(k_y, q_y) = (1 \pm \cos[\Theta_{n,n'}(k_y, q_y)])/2$ as obtained in Ref.[26]. For the opposite limiting case of a dice lattice, however, we have $\mathbb{O}_{\pm 1 \leftrightarrow 1}^{n,n'}(k_y, q_y) = (1 \pm \cos[\Theta_{n,n'}(k_y, q_y)])^2/4$.

Here, we would like to emphasize that the overlaps discussed above result in crucial difference between plasmons in nanoribbons and bulk $\alpha - \mathcal{T}_3$ materials. The angle $\Theta_{n,n'}(k_y, q_y)$ between the wave vectors k_y and $k_y + q_y$ (i.w., either 0 or π) is quantized in a nanoribbon due to W_R-dependent quantization of allowable values for the transverse wave number $\xi_{n(n')}$, while the longitudinal wave numbers k_y and $k_y + q_y$ are always directed along the $y-$axis. Since the largest contribution to the polarization function comes from several of the lowest subbands with the minimal values for $\xi_{n(n')}$, the resulting angles $\Theta_{n,n'}(k_y, q)$ are often close to 0 or π so that a large number of relevant overlaps are equal to either 1 or 0, especially in the long wavelength limit with $q_y \to 0$. This nanoribbon-specific feature is drastically different from that of a bulk material.

Results and discussion

We begin our calculations for an armchair $\alpha - \mathcal{T}_3$ nanoribbon with metallic (gapless) bandstructure. The lowest and the next subbands above are assumed well separated from each other. We adopt a single-subband model for calculating the polarization function previously employed for graphene nanoribbon[26,86,87]. Such a model could be considered sufficiently accurate for a narrow ribbon with low electron doping E_F.

The transverse wave vector ξ_n at the Fermi surface becomes negligibly small, and then the angle θ_n associated with the wave vector $\{\xi_n, k_y\}$ becomes

$$\theta_n(k_y) \approx \begin{cases} -\pi/2 & \text{if } k_y < 0, \\ \pi/2 & \text{if } k_y > 0. \end{cases} \tag{17}$$

The angle $\Theta_{n,n'}(k_y, q_y)$ between two states $\{\xi_n, k_y\}$ and $\{\xi_n, k_y + q_y\}$ is

$$\Theta_{n,n'}(k_y, q_y) = \begin{cases} -\pi & \text{if} \quad k_y > 0 \text{ and } k_y + q_y < 0, \\ 0 & \text{if} \quad k_y(k_y + q_y) > 0, \\ \pi & \text{if} \quad k_y < 0 \text{ but } k_y + q_y > 0. \end{cases} \qquad (18)$$

In all cases, this leads to $\sin[\Theta_{n,n'}(k_y, q_y)] = 0, \mathbb{O}_{0\leftrightarrow 1}^{n,n'}(k_y, q_y) = 0$, and $\mathbb{O}_{\pm 1 \leftrightarrow 1}^{n,n'}(k_y, q_y) = (1 \pm \cos[\Theta_{n,n'}(k_y, q_y)])^2/4$ is either 0 or 1 due to

$$\mathbb{O}_{\sigma \leftrightarrow \sigma'}^{N_0, N_0}(k_y, k_y + \beta q) = \delta_{\sigma\sigma', \text{sign}[k_y \cdot (k_y + \beta q)]}, \qquad (19)$$

where $\sigma, \sigma' \neq 0$ and $\beta = \pm 1$.

For $T = 0$, the Fermi distribution functions are reduced to (13), and the polarizability could be presented as

$$\Pi^{(0)}(q, \omega) = -\chi_\infty^{(-)}(q, \omega) + \sum_{\beta = \pm 1} \chi_{E_F}^{(\beta)}(q, \omega), \qquad (20)$$

where the first term corresponds to zero doping (which is possible only for graphene with $\phi = 0$ due to the momentum degeneracy in the flat band) and is equal to

$$\chi_\infty^{(-)}(q, \omega) = g_s \sum_{\beta = \pm 1} \int \frac{dk_y}{2\pi} \frac{\mathbb{O}_{-1 \leftrightarrow +1}^{N_0, N_0}(k_y, k_y + q)}{\varepsilon_{N_0}(k_y) + \varepsilon_{N_0}(k_y + q) + \beta \, \omega}. \qquad (21)$$

The expansion of (20) looks similar to that for bulk graphene[19]. However, there is a crucial difference, i.e., the integration is performed only over one variable k_y (there is no angular integral). The two terms with $k \pm q$ in the sum in Eq. (21) are substantially different and cannot replace one another. For that reason, there is no unified analytic expression for all three terms in Eq. (20). The two remaining terms of Eq. (20) which appear only for finite doping are

$$\chi_{E_F}^{(\rho = \pm)}(q, \omega) = g_s \sum_{\beta = \pm} \int \frac{dk_y}{2\pi} \mathbb{O}_{\rho \leftrightarrow +1}^{N_0, N_0}(k_y, k_y + \beta q) \frac{\Theta\left[E_F - \varepsilon_{N_0}(k_y)\right]}{\varepsilon_{N_0}(k_y) - \rho \, \varepsilon_{N_0}(k_y + \beta q) + \beta \, \omega} \qquad (22)$$

The zero-doping term in Eq. (21) is immediately evaluated as

$$\chi_\infty^{(-)}(q, \omega) = -\frac{2\gamma_0}{\pi} \frac{q^2}{\omega^2 - (\gamma_0 q)^2}, \qquad (23)$$

and the other two terms in the expansion (20) are

$$\chi_{E_F}^{(-)}(q, \omega) = g_s \sum_{\beta = \pm} \int \frac{dk_y}{2\pi} \Theta\left[\frac{E_F}{\gamma_0} - |k_y|\right] \Theta[-\beta k_y(k_y + \beta q)] (\gamma_0 q + \beta \omega)^{-1} = -\frac{2\gamma_0 q}{\pi} \frac{\text{Min}(q, k_F)}{\omega^2 - (\gamma_0 q)^2}. \qquad (24)$$

and

$$\chi_{E_F}^{(+)}(q, \omega) = \frac{2\gamma_0}{\pi} \frac{k_F q}{\omega^2 - q^2} \left\{ 1 - \left(1 - \frac{q}{k_F}\right) \Theta[k_F - q] \right\}, \qquad (25)$$

which is equivalent to

$$\chi_{E_F}^{(+)}(q, \omega) = \frac{2\gamma_0 q}{\pi} \frac{\text{Min}(q, k_F)}{\omega^2 - (\gamma_0 q)^2} = -\chi_{E_F}^{(-)}(q, \omega), \qquad (26)$$

which was demonstrated in Sect. III of the Supplementary Information. We have found that the two terms corresponding to finite doping always cancel each other. This is equivalent to finite-temperature behavior discussed in Ref.[87] but differs from the results of Ref.[86] for graphene. Our final result in Eq. (21) for the polarization function shows no dependence on α and is the same as for GNR's[86,89]. The plasmon mode $\Omega_p(q_y)$ in the long-wavelength limit is immediately obtained as[89]

$$\Omega_p(q_y) = \frac{\gamma_0}{\hbar} \sqrt{-q_y^2 \ln(q_y W_R)}, \qquad (27)$$

which also does not depend on the doing level E_F and parameter α due to the absence of such dependence in Coulomb matrix elements (14).

In most realistic cases, however, the cross momentum $\xi_n \neq 0$ and all the wave function overlaps are finite and depend on q_y. This occurs if $\Theta_{n,n}(k_y, q_y)$ differs from 0 and π which is achieved for a finite gap or ξ_n disregarding the ribbon width W_R. However, for large W_R, it approaches bulk $\alpha - \mathcal{T}_3$ since the change in ξ_n with n decreases ($\propto 1/W_R$). In this case, the dependence on q_y in the range of $q_y/k_F \leq 1$ also varies with k_y and its dependence in $\xi_n(k_y)$, as seen in Fig. 3.

The difference between graphene and other types of $\alpha - \mathcal{T}_3$ lattices arises from transitions from/to the flat band[22]. Since the $0 \leftrightarrow 1$ overlap contains the factor $\sin^2(2\phi) \sin^2[\Theta_{n,n}(k_y, q_y)]$, it will be suppressed as $\alpha \simeq 0$ or $\phi \simeq 0$, i.e., for all materials resembling graphene and small ξ_n in a wide ribbon. Consequently, we conclude that the α dependence of overlap in the range $q_y/k_F \ll 1$ becomes appreciable only for a sufficiently wide ribbon, as
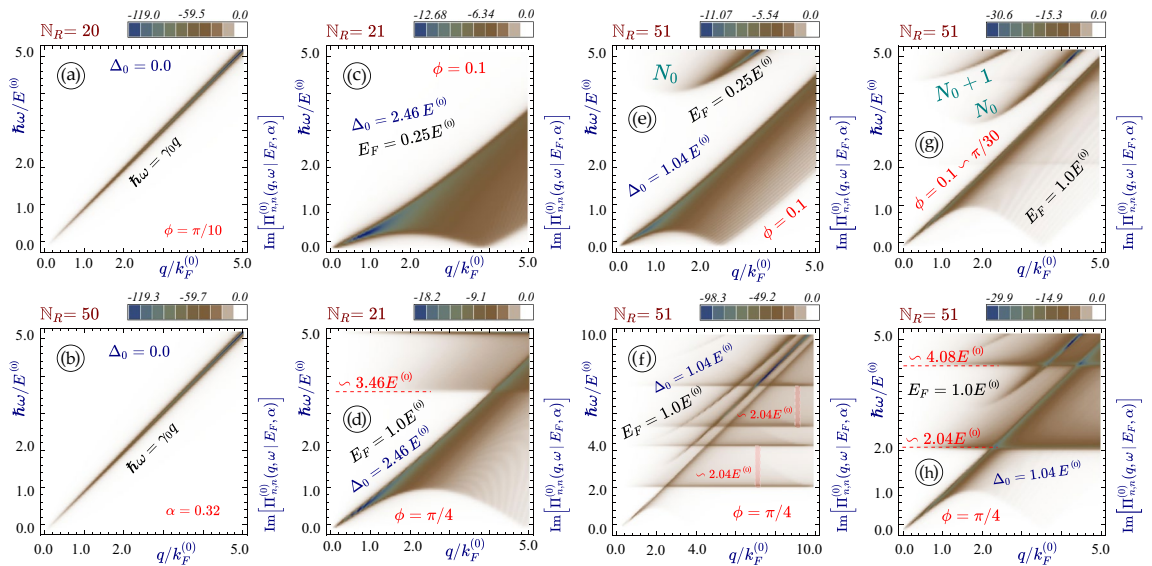
Figure 4. Single-particle excitation spectrum in $\alpha - \mathcal{T}_3$ nanoribbons. All panels (**a**) through (**h**) present density plots as functions of frequency ω and q_y for the imaginary part of the non-interacting *intra-subband* polarization function $\Pi_{n,n}^{(0)}(q_y, \omega \mid E_F, \alpha)$ with chosen widths $\mathbb{N}_R = 20, 21, 50$ and 51. The material bandgap $\Delta_0/E^{(0)}$ determined by $\mathbb{N}_R$ is equal to zero in (**a**), (**b**) but 2.46 in (**c**), (**d**) and 1.04 in (**e**)–(**h**), respectively. The relative hopping parameter α was chosen as $\alpha \backsim \phi = 0.1$ for panels (**c**), (**e**) and (**g**), $\alpha = 0.32$ (or $\phi = \pi/10$) for (**a**) and (**b**) and $\phi = \pi/4$ (a dice lattice) for the remaining plots (**d**), (**f**) and (**h**).

demonstrated in Fig. 3b through Fig. 3c. On the other hand, if $q_y/k_F \backsim 1$ is achieved, the α dependence of the overlap is noticeable for all ribbon widths (e.g., see Fig. 3d).

The imaginary part of the intra-subband polarization function for armchair nanoribbon is presented in Fig. 4. If there is no bandgap (metallic case, see Fig. 4a,b), the single-particle excitation spectrum is only a strong peak around the main diagonal $\hbar\omega = \gamma_0 q_y$. This dissipation is slightly enhanced with increasing ribbon width since more electron subbands are occupied for the same doping value.

A very different situation occurs if $\mathbb{N}_R$ is chosen such that the gap $\Delta_0 > 0$. The previously narrow single-particle excitation region now occupies a sizable area in the q_y - ω plane, as shown in panels (*a*) through (*h*) of Fig. 4. It is split into two or more broad sub-domains bounded by semi-parabolic edges and separated by a gap, and the whole picture becomes qualitatively similar to bulk gapped graphene[18] or $\alpha - \mathcal{T}_3$[72]. The lower domain corresponds to the intra-band (conduction-to-conduction) excitations while the upper one - to the inter-band (valence-to-conduction and vice versa) ones. Meanwhile, the magnitudes of dissipation within all the intra- and inter-band damping regions are modified greatly by the ribbon width (compare panels (*c*) and (*d*)).

Another area of finite $\mathrm{Im}\left[\Pi^{(0)}(q, \omega)\right]$ is uniformly distributed above the Fermi level. It arises due to inter-band electron transitions between the valence and flat bands. It is seen in all cases (panels (*d*), (*f*) and (*h*)) when $\alpha > 0$. We conclude that the difference between $\alpha - \mathcal{T}_3$ and graphene ribbons is substantial for any ribbon width if a finite gap is present. The lower boundary of this area is found at frequency $\hbar\omega \simeq E_F + \Delta_0$ which corresponds to the energy separation between the flat band (zero-energy level) and the actual Fermi level above the gap. We also noticed that $0 \leftrightarrow 1$ particle-hole mode consists of multiple separate sub-areas corresponding to the transitions from and to the various discrete energy subbands (see panels (*f*) and (*h*) shown for the same nanoribbon but in different ranges of ω and q).

The plasmon frequencies for armchair nanoribbon with chosen ribbon widths $\mathbb{N}_R$ and bandgaps Δ_0 is shown in Fig. 5. as the peaks of the loss function $\mathbb{S}(q_y, \omega \mid E_F, \alpha)$. The loss function, or the spectral function, is defined as $\mathrm{Im}[1/\epsilon(q_y, \omega)]$ through our calculated dielectric function $\epsilon(q_y, \omega)$, which has been utilized for graphically plotting $\mathrm{Re}[\epsilon(q_y, \omega)] = 0$ or maximum values of $\mathrm{Im}[1/\epsilon(q_y, \omega + i\delta)]$ with $\delta/\omega \ll 1$ within the (q_y, ω)-plane[91,92]. On the other hand, the physically-defined loss function $\mathrm{Im}[\mathcal{S}(q_\parallel, \omega)]$ has been widely employed for describing power absorption of electron beam either parallel or perpendicular to the surface of an electronic system, where $\mathcal{S}(q_\parallel, \omega)$ is the surface response function, related to the inverse dielectric-function matrix $\overleftrightarrow{\epsilon}^{-1}(q_\parallel, \omega)$ of electronic system[93,94].

As $\Delta_0 = 0$, for a relatively narrow ribbon in Fig. 5a, the group velocity of intra-subband plasmon mode is increased greatly in comparison with a wider ribbon in Fig. 5c. When Δ_0 becomes finite, the group velocity of intra-subband plasmon mode is reduced significantly, as shown in panels (*b*) and (*d*), similar to $\simeq \left(1 - \Delta_0^2/E_F^2\right)$ dependence for the plasmon group velocity in bulk. In comparison with panel (*b*), a wider ribbon in panel (*d*) further develops a unique concave-to-convex feature in plasmon dispersion, resembling bulk material and meanwhile acquiring an increased dissipation at this "crossing" point. For finite α, the plasmon becomes strongly damped at the Fermi level (above the bandgap), as shown in panels (*e*) and (*f*) of Fig. 5. Figures 4 and 5 are presented in a way that in most cases the particle-hole modes and the plasmons are demonstrated for the same nanoribbons (panels (*a*) and (*b*)) in both graphs and some others).
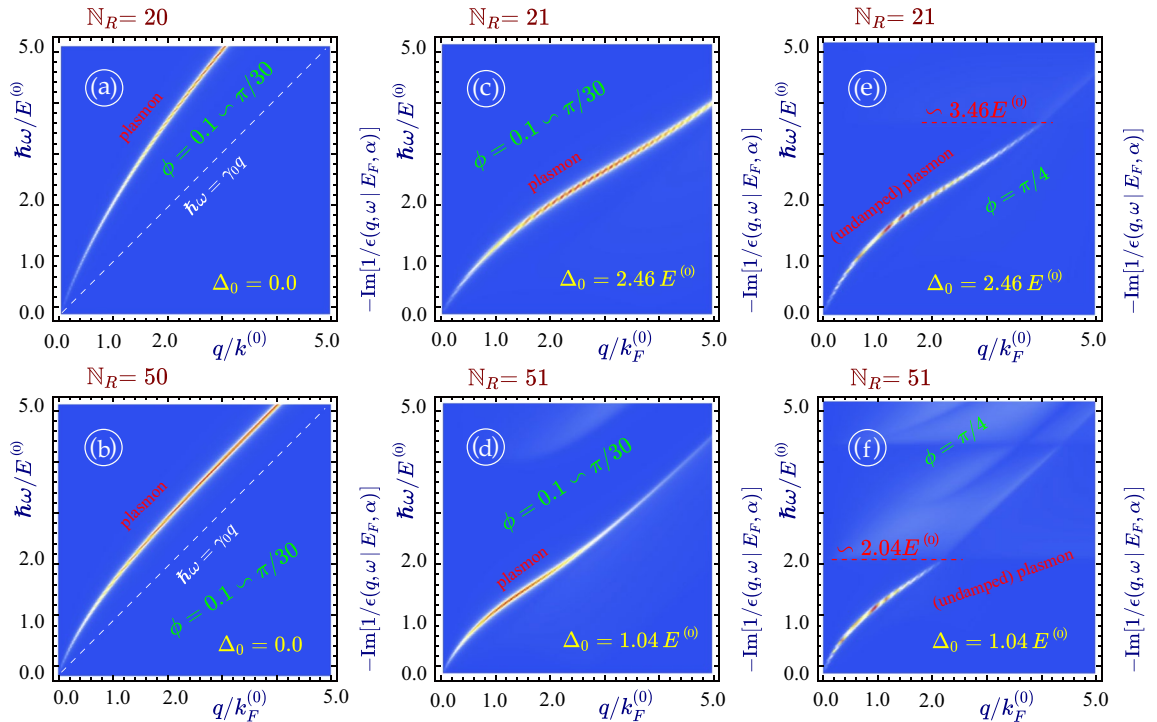
Figure 5. Plasmon excitations in $\alpha - \mathcal{T}_3$ nanoribbons. All panels (**a**) through (**d**) display density plots of the spectral loss function $\mathbb{S}(q_y, \omega \mid E_F, \alpha) = -\text{Im}\left[1/\epsilon\left(q_y, \omega \mid E_F, \alpha\right)\right]$ as functions of ω and q_y with $\mathbb{N}_R = 20, 21, 50$ and 51. The undamped plasmon excitations correspond to sharp peaks of the loss function (ideally, $\mathbb{S} \to \infty$), therefore, the colorbars were not added to these panels. The values of the material bandgap are determined solely by the width of a nanoribbon and are exactly the same as we have for Fig. 4. The plasmon dispersions in (**a**) and (**b**) are related to metallic electronic spectra (**a**) and (**c**). However, they are to semiconducting ones in all other panels. Parameter α was chosen as $\pi/4$ (a dice lattice) for the lowest panels (**e**) and (**f**) but $\alpha \backsim \phi = 0.1$ for all the other plots. Panel (**f**) shows the same situation as (**h**) but for a larger (doubled) ranges of q and ω.

The dielectric function is defined as determinant of the dielectric tensor (10), where the Coulomb potential was defined in Eq. (14) as $V_0^0(q_y) \backsim e^2/(2\epsilon_0\epsilon_r) K_0(|q_y|W_R) \simeq -2\pi\alpha_\epsilon \ln(|q_y|W_R) \sim 2\pi\alpha_\epsilon/(|q_y|W_R)$. The dimensionless dielectric constant $\alpha_\epsilon = e^2/(4\pi\epsilon_0\epsilon_r) k_F^{(0)}/E^{(0)} \simeq 1.0$ was chosen in our computation, corresponding to $\epsilon_r = 2.4$ for SiO_2 substrate which is normally used for the plasmon calculation in graphene[19]. The role of background dielectric constant ϵ_r is certainly shaping out the plasmon branch which is very well seen in the long-wave limit, where $\Omega_p \backsim \sqrt{\alpha_\epsilon} \backsim 1/\sqrt{\epsilon_r}$, i.e., a larger ϵ_r leads to a smaller plasmon Ω_p for fixed wave number q_y.

For a metallic ribbon with no gap and for a reasonably small $\mathbb{N}_R < 100$, we found that the plasmon dispersions remain the same for graphene and all other types of $\alpha - \mathcal{T}_3$ materials including a dice lattice. The one-subband model for the polarizability showing no doping or α dependence seems to work well for all such ribbons (zero gap and a relatively small width). In a wide ribbon, however, many subbands need to be taken into account since a few of them will be populated under electron doping. We also need to keep in mind that one cannot apply the Dirac Hamiltonian approximation for bulk to a very narrow ribbon so that the previously addressed situation with low doping and large subband separation is transparent but very limited and cannot be employed for most realistic problems. The situation becomes drastically different if a gap is present. Both inter- and intra-band portions of particle-hole modes are split into two separate regions in the ω-q_y plane and a strong dependence on α is observed irrespective of the ribbon width.

Figure 6 demonstrates the effect due to relative hopping played by α in a very wide nanoribbon with $\mathbb{N}_R = 200$. The separation between two adjacent subbands decreases to $\backsim 0.7E^{(0)}$ in order to occupy multiple subbands for chosen doping to approach bulk material. As a starting point, we first examine a (unrealistic) situation, as in Fig. 6a, by setting all overlaps to unity. In this case, we are able to see contributions from all transitions as well as a strong dissipation peak near the main diagonal $\hbar\omega = \gamma_0 q$.

When only the flat band $0 \leftrightarrow 1$ transitions are considered, we expect Landau damping of plasmons due to the presence of particle-hole modes within the region $\hbar\omega \geq E_F$, as seen in Fig. 6b, which appears as a layer structured because of the nature of discrete subbands. Additionally, its contribution to $\text{Im}\left[\Pi_{n,n}^{(0)}(q_y, \omega)\right]$ at $\hbar\omega = E_F$ is about half its maximum, and it increases with ω since more subband contributions are included. Meanwhile, the flat-band dissipation becomes stronger with increasing wave vector q_y for chosen ω. Such strong plasmon damping at relatively low q_y is responsible for the significant change in plasmon dispersions from graphene to $\alpha - \mathcal{T}_3$ for both bulk and nanoribbon, as can be easily verified from Fig. 6e and f, where the plasmon branch also exhibits a unique shape for pinching when $\hbar\Omega_p(q_y)/E_F = 1$ at the point where $q_y/k_F^{(0)} = 1$. Specifically, for a dice lattice we display both its plasmon dispersion in Fig. 6d and dissipation in Fig. 6c, where all intra-subband and inter-subband transitions among nine subbands have been considered. The trace of Landau
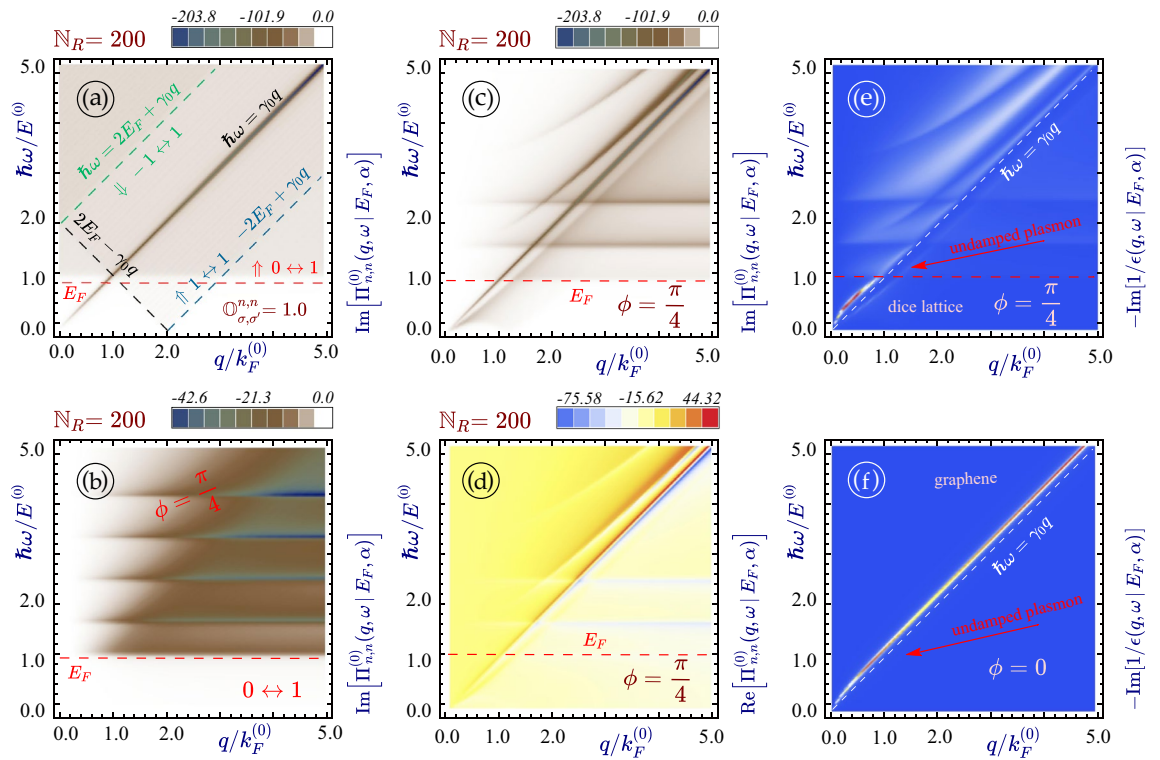
Figure 6. Intra-subband polarization function $\Pi_{n,n}^{(0)}(q_y, \omega \mid E_F, \alpha)$, single-particle excitation spectrum and plasmon dispersion for a very wide metallic nanoribbon with $\mathbb{N}_R = 200$ and $N_0 = (\mathbb{N}_R + 1)/3 = 67$. Panel (**a**) presents a (unrealistic) case when all overlaps $\mathbb{O}_{\sigma_1 \leftrightarrow \sigma_2}^{n,n'}(k_y, q_y)$ ($\sigma_{1,2} = 0, \pm 1$) are set to unity with an equal contribution to $\Pi_{n,n'}^{(0)}(q_y, \omega \mid E_F, \alpha)$. Panel (**b**) shows the contribution of transitions from and to the flat band *only*, i.e., setting $\mathbb{O}_{\pm 1 \leftrightarrow \pm 1}^{n,n}(k_y, q) = 0$, for a dice lattice with $\phi = \pi/4$. Panels (**c**) and (**d**) display the imaginary and real parts of $\Pi_{n,n}^{(0)}(q_y, \omega \mid E_F, \alpha)$ for a dice lattice when all nine intra-band and inter-band transitions are included. Panels (**e**) and (**f**) exhibit the calculated plasmon dispersions by tracking peaks of a spectral-loss function $\mathbb{S}(q_y, \omega \mid E_F, \alpha)$ for a dice lattice and graphene with $\phi = \pi/4$ and $\phi = 0$, separately. Other parameters are the same as those in Fig. 2.

damping of plasmons from flat-band $0 \leftrightarrow 1$ transitions is clearly visible in Fig. 6c, in addition to plasmon damping due to intra-subband and inter-subband transitions.

We find that the nanoribbon plasmon frequency is much less sensitive to the electron doping or Fermi energy E_F than in the case of bulk graphene (or a dice lattice), as demonstrated by the red-solid and black-dashed curves in Fig. 7a. As we showed above, the polarization function is completely independent of E_F in one-subband approximation which represents the dominant contribution for narrow ribbons with metallic dispersions. In the general case, the polarization function becomes independent of E_F if $q > E_F/\gamma_0$, as explained by inset (i1) of Fig. 7a. At the same time, the strength of pinching in a wide nanoribbon can be enhanced by increasing α from zero to unity, as seen in Fig. 7b.

Summary and remarks

In this paper, we have calculated the dynamical polarization function, dielectric tensor, the resulting plasmon dispersions and Landau damping for various types of $\alpha - \mathcal{T}_3$ nanoribbons with armchair edge termination. Armchair nanoribbons are distinguished because their longitudinal k_y and transverse ξ_n components of the electron momentum are not coupled to each other, the wave functions and their overlaps are similar to those for the bulk except for the quantized ξ_n and the energy dispersions, as well as the valley mixing.

The plasmon excitations in a nanoribbon and their Landau damping (single-particle excitation spectrum) are mainly determined by the energy bandgap in the electron dispersions which directly depend on the width of the ribbon or, specifically, on the number $\mathbb{N}_R$ of atomic rows across the ribbon. The ribbon is metallic (zero bandgap between the valence, flat and conduction bands) if $\mathbb{N}_R + 1$ is an integer multiple of 3. For all other numbers $\mathbb{N}_R$, the ribbon has a $\backsim 1/\mathbb{N}_R$ gap even though the bulk bandstructure is metallic which holds true for the ribbons made of all $\alpha - \mathcal{T}_3$ materials including graphene and dice.

The main focus of our investigation has been to identify the role of the relative hopping parameter α or the distinctions between the plasmon modes in nanoribbons based on various $\alpha - \mathcal{T}_3$ materials. These materials, specifically a dice lattice, stand out due to the presence of an additional dispersionless zero-energy band in the electron dispersions, and the electron transitions to and from this flat band. The overlaps of the transitions between the valence and partially occupied conduction band are also affected by α. An additional particle hole mode above the Fermi level is also observed for all nanoribbons with a finite gap, however, its lower boundary
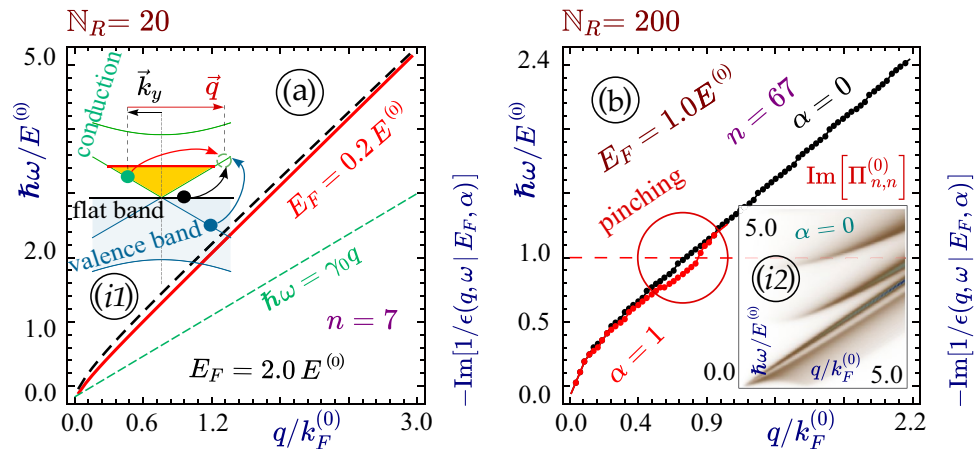
Figure 7. Panel (**a**) presents plasmons for different electron densities, correspond to $E_F/E^{(0)} = 0.2$ (black) and 2.0 (red) in a narrow ribbon of $\mathbb{N}_R = 20$. Panel (**b**) displays plasmons for graphene (black) and a dice lattice (red) in a wide nanoribbon of $\mathbb{N}_R = 200$ for $E_F/E^{(0)} = 1.0$. Inset (*i1*) in (**a**) illustrates all allowed transitions in a narrow metallic electron-doped $\alpha - \mathcal{T}_3$ ribbon, while inset (*i2*) in (**b**) exhibits single-particle excitation spectrum in a wide metallic graphene nanoribbon. Other parameters are the same as those in Fig. 2.

is shifted up to $E_F + \Delta_0$ since the energy separation between the zero-energy flat band and the Fermi energy should also include the gap.

The most substantial difference between bulk $\alpha - \mathcal{T}_3$ and nanoribbons stems from the quantization of the energy bandstructure. The discernible contribution from various energy subbands is clearly seen in separate regions of the single-particle excitation spectrum. Another feature of a nanoribbon is that the overlaps only depend on a single-subband index *n*, in a narrow ribbon, they become either equal or close to zero for some transitions which otherwise would be dominant in a bulk material so that in many cases the terms contributing to the polarization disappear. Finally, the dielectric tensor of a nanoribbon is such that only intra-subband ($n \leftrightarrow n$) transitions need to be included in the polarizability.

In a nutshell, we have performed a comprehensive study on the plasmon excitations in an $\alpha - \mathcal{T}_3$ nanoribbon. We discovered some very distinctive features of plasmon dispersion and the distribution of its finite Landau damping with respect to the width of a ribbon, absence/presence of a bandgap, electron doping density and a phase of the $\alpha - \mathcal{T}_3$ lattice. These previously unreported plasmonic properties have the potential of being widely employed in next-generation nanoribbon-based electronic, optical and plasmonic quantum devices.

References

1. Gröning, O. *et al.* Engineering of robust topological quantum phases in graphene nanoribbons. *Nature* **560**, 209 (2018).
2. Cao, T., Zhao, F. & Louie, S. G. Topological phases in graphene nanoribbons: Junction states, spin centers, and quantum spin chains. *Phys. Rev. Lett.* **119**, 076401 (2017).
3. Kitaev, A. Y. Unpaired Majorana fermions in quantum wires. *Phys. Uspekhi* **44**, 131 (2001).
4. Pfeiffer, M. *et al.* Enhanced light–matter interaction of aligned armchair graphene nanoribbons using arrays of plasmonic nano-antennas. *2D Mater.* **5**, 045006 (2018).
5. Sevinçli, H., Topsakal, M. & Ciraci, S. Superlattice structures of graphene-based armchair nanoribbons. *Phys. Rev. B* **78**, 245402 (2008).
6. Richter, N. *et al.* Charge transport mechanism in networks of armchair graphene nanoribbons. *Sci. Rep.* **10**, 1 (2020).
7. Fei, Z. *et al.* Edge and surface plasmons in graphene nanoribbons. *Nano Lett.* **15**, 8271 (2015).
8. Karimi, F. & Knezevic, I. Plasmons in graphene nanoribbons. *Phys. Rev. B* **96**, 125417 (2017).
9. Xia, S.-X., Zhai, X., Wang, L.-L., Lin, Q. & Wen, S.-C. Localized plasmonic field enhancement in shaped graphene nanoribbons. *Opt. Express* **24**, 16336 (2016).
10. Sarsen, A. & Valagiannopoulos, C. Robust polarization twist by pairs of multilayers with tilted optical axes. *Phys. Rev. B* **99**, 115304 (2019).
11. Gomez, C. V., Pisarra, M., Gravina, M., Pitarke, J. M. & Sindona, A. Plasmon modes of graphene nanoribbons with periodic planar arrangements. *Phys. Rev. Lett.* **117**, 116801 (2016).
12. Khaliji, K. *et al.* Plasmonic gas sensing with graphene nanoribbons. *Phys. Rev. Appl.* **13**, 011002 (2020).
13. Hu, F. *et al.* Imaging the localized plasmon resonance modes in graphene nanoribbons. *Nano Lett.* **17**, 5423 (2017).
14. Xia, S.-X., Zhai, X., Wang, L.-L. & Wen, S.-C. Plasmonically induced transparency in double-layered graphene nanoribbons. *Photonics Res.* **6**, 692 (2018).
15. Grigorenko, A. N., Polini, M. & Novoselov, K. Graphene plasmonics. *Nat. Photonics* **6**, 749 (2012).
16. Garcia de Abajo, F. J. Graphene plasmonics: Challenges and opportunities. *ACS Photonics* **1**, 135 (2014).
17. Hwang, E. & Sarma, S. D. Dielectric function, screening, and plasmons in two-dimensional graphene. *Phys. Rev. B* **75**, 205418 (2007).
18. Pyatkovskiy, P. Dynamical polarization, screening, and plasmons in gapped graphene. *J. Phys. Condens. Matter* **21**, 025506 (2008).

19. Wunsch, B., Stauber, T., Sols, F. & Guinea, F. Dynamical polarization of graphene at finite doping. *New J. Phys.* **8**, 318 (2006).
20. Iurov, A., Gumbs, G., Huang, D. & Balakrishnan, G. Thermal plasmons controlled by different thermal-convolution paths in tunable extrinsic Dirac structures. *Phys. Rev. B* **96**, 245403 (2017a).
21. Gumbs, G., Balassis, A., Iurov, A. & Fekete, P. Strongly localized image states of spherical graphitic particles. *Sci. World J.* **2014** https://doi.org/10.1155/2014/726303 (2014).
22. Malcolm, J. & Nicol, E. Frequency-dependent polarizability, plasmons, and screening in the two-dimensional pseudospin-1 dice lattice. *Phys. Rev. B* **93**, 165433 (2016).
23. Iurov, A., Gumbs, G., Huang, D. & Zhemchuzhna, L. Controlling plasmon modes and damping in buckled two-dimensional material open systems. *J. Appl. Phys.* **121**, 084306 (2017b).
24. Gumbs, G., Iurov, A., Huang, D. & Pan, W. Tunable surface plasmon instability leading to emission of radiation. *J. Appl. Phys.* **118**, 054303 (2015).
25. Gonçalves, P. A. D. & Peres, N. M. *An Introduction to Graphene Plasmonics* (World Scientific, 2016).
26. Brey, L. & Fertig, H. Electronic states of graphene nanoribbons studied with the Dirac equation. *Phys. Rev. B* **73**, 235411 (2006).
27. Andersen, D. R. & Raza, H. Plasmon dispersion in semimetallic armchair graphene nanoribbons. *Phys. Rev. B* **85**, 075425 (2012).
28. Hancock, Y., Uppstu, A., Saloriutta, K., Harju, A. & Puska, M. J. Generalized tight-binding transport model for graphene nanoribbon-based systems. *Phys. Rev. B* **81**, 245402 (2010).
29. Rodrigues, J. N. *et al.* Zigzag graphene nanoribbon edge reconstruction with Stone–Wales defects. *Phys. Rev. B* **84**, 155435 (2011).
30. Raza, H. & Kan, E. C. Armchair graphene nanoribbons: Electronic structure and electric-field modulation. *Phys. Rev. B* **77**, 245434 (2008).
31. Kimouche, A. *et al.* Ultra-narrow metallic armchair graphene nanoribbons. *Nat. Commun.* **6**, 1 (2015).
32. Zheng, H., Wang, Z., Luo, T., Shi, Q. & Chen, J. Analytical study of electronic structure in armchair graphene nanoribbons. *Phys. Rev. B* **75**, 165414 (2007).
33. Zhao, S. *et al.* Optical imaging and spectroscopy of atomically precise armchair graphene nanoribbons. *Nano Lett.* **20**, 1124 (2020).
34. Thongrattanasiri, S., Manjavacas, A. & Garcia de Abajo, F. J. Quantum finite-size effects in graphene plasmons. *ACS Nano* **6**, 1766 (2012).
35. Kibis, O. Metal-insulator transition in graphene induced by circularly polarized photons. *Phys. Rev. B* **81**, 165433 (2010).
36. Kunold, A., Sandoval-Santana, J., Ibarra-Sierra, V. & Naumis, G. G. Floquet spectrum and electronic transitions of tilted anisotropic Dirac materials under electromagnetic radiation: Monodromy matrix approach. *Phys. Rev. B* **102**, 045134 (2020).
37. Sandoval-Santana, J., Ibarra-Sierra, V., Kunold, A. & Naumis, G. G. Floquet spectrum for anisotropic and tilted Dirac materials under linearly polarized light at all field intensities. *J. Appl. Phys.* **127**, 234301 (2020).
38. Rozhkov, A., Savel'ev, S. & Nori, F. Electronic properties of armchair graphene nanoribbons. *Phys. Rev. B* **79**, 125420 (2009).
39. Politano, A. & Chiarello, G. Plasmon modes in graphene: Status and prospect. *Nanoscale* **6**, 10927 (2014).
40. Ooi, K. J., Chu, H. S., Ang, L. K. & Bai, P. Mid-infrared active graphene nanoribbon plasmonic waveguide devices. *JOSA B* **30**, 3111 (2013).
41. Chen, J. *et al.* Optical nano-imaging of gate-tunable graphene plasmons. *Nature* **487**, 77 (2012).
42. Li, Y., Tantiwanichapan, K., Swan, A. K. & Paiella, R. Graphene plasmonic devices for terahertz optoelectronics. *Nanophotonics* **9**, 1901 (2020).
43. Chen, Z. *et al.* Synthesis of graphene nanoribbons by ambient-pressure chemical vapor deposition and device integration. *J. Am. Chem. Soc.* **138**, 15488 (2016).
44. Zhang, X. *et al.* Structure and photoluminescence of ZnSe nanoribbons grown by metal organic chemical vapor deposition. *Appl. Phys. Lett.* **84**, 2641 (2004).
45. Talirz, L., Ruffieux, P. & Fasel, R. On-surface synthesis of atomically precise graphene nanoribbons. *Adv. Mater.* **28**, 6222 (2016).
46. Xu, W. & Lee, T.-W. Recent progress in fabrication techniques of graphene nanoribbons. *Mater. Horiz.* **3**, 186 (2016).
47. Cai, J. *et al.* Atomically precise bottom–up fabrication of graphene nanoribbons. *Nature* **466**, 470 (2010).
48. Tan, C.-Y. *et al.* Anisotropic longitudinal optical conductivities of tilted Dirac bands in $1T'-MoS_2$. *Phys. Rev. B* **103**, 125425 (2021).
49. Liu, Y. *et al.* Van der Waals heterostructures and devices. *Nat. Rev. Mater.* **1**, 1 (2016).
50. Leykam, D., Andreanov, A. & Flach, S. Artificial flat band systems: From lattice models to experiments. *Adv. Phys. X* **3**, 1473052 (2018).
51. Iurov, A., Gumbs, G. & Huang, D. Peculiar electronic states, symmetries, and Berry phases in irradiated $\alpha - \mathcal{T}_3$ materials. *Phys. Rev. B* **99**, 205135 (2019).
52. Dey, B. & Ghosh, T. K. Photoinduced valley and electron-hole symmetry breaking in $\alpha - \mathcal{T}_3$ lattice: The role of a variable Berry phase. *Phys. Rev. B* **98**, 075422 (2018).
53. Dey, B. & Ghosh, T. K. Floquet topological phase transition in the $\alpha - \mathcal{T}_3$ lattice. *Phys. Rev. B* **99**, 205429 (2019).
54. Gorbar, E., Gusynin, V. & Oriekhov, D. Gap generation and flat band catalysis in dice model with local interaction. *Phys. Rev. B* **103**, 155155 (2021).
55. Cunha, S. *et al.* Band-gap formation and morphing in $\alpha - \mathcal{T}_3$ superlattices. *Phys. Rev. B* **104**, 115409 (2021).
56. Islam, S. F. & Zyuzin, A. Photoinduced interfacial chiral modes in threefold topological semimetal. *Phys. Rev. B* **100**, 165302 (2019).
57. Islam, S. F. & Saha, A. Driven conductance of an irradiated semi-Dirac material. *Phys. Rev. B* **98**, 235424 (2018).
58. Bercioux, D., Urban, D., Grabert, H. & Häusler, W. Massless Dirac–Weyl fermions in a $\mathcal{T}_3$ optical lattice. *Phys. Rev. A* **80**, 063603 (2009).
59. Weekes, N., Iurov, A., Zhemchuzhna, L., Gumbs, G. & Huang, D. Generalized WKB theory for electron tunneling in gapped $\alpha - \mathcal{T}_3$ lattices. *Phys. Rev. B* **103**, 165429 (2021).
60. Wu, Y.-R. & Zhang, Y.-C. Superfluid states in $\alpha - \mathcal{T}_3$ lattice. *Chin. Phys. B* https://iopscience.iop.org/article/10.1088/1674-1056/abea8a (2021).
61. Kovács, Á. D., Dávid, G., Dóra, B. & Cserti, J. Frequency-dependent magneto-optical conductivity in the generalized $\alpha - \mathcal{T}_3$ model. *Phys. Rev. B* **95**, 035414 (2017).
62. Ye, X., Ke, S.-S., Du, X.-W., Guo, Y. & Lü, H.-F. Quantum tunneling in the $\alpha - \mathcal{T}_3$ model with an effective mass term. *J. Low Temp. Phys.* 1–12 https://doi.org/10.1007/s10909-020-02440-3 (2020).
63. Gorbar, E., Gusynin, V. & Oriekhov, D. Electron states for gapped pseudospin-1 fermions in the field of a charged impurity. *Phys. Rev. B* **99**, 155124 (2019).
64. Anwar, F., Iurov, A., Huang, D., Gumbs, G. & Sharma, A. Interplay between effects of barrier tilting and scatterers within a barrier on tunneling transport of Dirac electrons in graphene. *Phys. Rev. B* **101**, 115424 (2020).
65. Urban, D. F., Bercioux, D., Wimmer, M. & Häusler, W. Barrier transmission of Dirac-like pseudospin-one particles. *Phys. Rev. B* **84**, 115136 (2011).
66. Illes, E. & Nicol, E. Klein tunneling in the $\alpha - \mathcal{T}_3$ model. *Phys. Rev. B* **95**, 235432 (2017).
67. Iurov, A., Zhemchuzhna, L., Fekete, P., Gumbs, G. & Huang, D. Klein tunneling of optically tunable Dirac particles with elliptical dispersions. *Phys. Rev. Res.* **2**, 043245 (2020a).
68. Wang, J., Liu, J. & Ting, C. Recovered minimal conductivity in the $\alpha - \mathcal{T}_3$ model. *Phys. Rev. B* **101**, 205420 (2020).
69. Islam, S. F. & Dutta, P. Valley-polarized magnetoconductivity and particle–hole symmetry breaking in a periodically modulated $\alpha - \mathcal{T}_3$ lattice. *Phys. Rev. B* **96**, 045418 (2017).
70. Zhou, X. Andreev reflection and Josephson effect in the $\alpha - \mathcal{T}_3$ lattice. arXiv preprint arXiv:2105.11070 (2021).

71. Mojarro, M., Ibarra-Sierra, V., Sandoval-Santana, J., Carrillo-Bastos, R. & Naumis, G. G. Electron transitions for Dirac Hamiltonians with flat bands under electromagnetic radiation: Application to the $\alpha - \mathscr{T}_3$ graphene model. *Phys. Rev. B* **101**, 165305 (2020).
72. Iurov, A., Zhemchuzhna, L., Dahal, D., Gumbs, G. & Huang, D. Quantum-statistical theory for laser-tuned transport and optical conductivities of dressed electrons in $\alpha - \mathscr{T}_3$ materials. *Phys. Rev. B* **101**, 035129 (2020b).
73. Biswas, T. & Ghosh, T. K. Dynamics of a quasiparticle in the $\alpha - \mathscr{T}_3$ model: Role of pseudospin polarization and transverse magnetic field on zitterbewegung. *J. Phys. Condens. Matter* **30**, 075301 (2018).
74. Biswas, T. & Ghosh, T. K. Magnetotransport properties of the $\alpha - \mathscr{T}_3$ model. *J. Phys. Condens. Matter* **28**, 495302 (2016).
75. Illes, E. & Nicol, E. Magnetic properties of the $\alpha - \mathscr{T}_3$ model: Magneto-optical conductivity and the Hofstadter butterfly. *Phys. Rev. B* **94**, 125435 (2016).
76. Illes, E., Carbotte, J. P. & Nicol, E. J. Hall quantization and optical conductivity evolution with variable Berry phase in the $\alpha - \mathscr{T}_3$ model. *Phys. Rev. B* **92**, 245401 (2015a).
77. Illes, E. *Properties of the $\alpha - \mathscr{T}_3$ Model*. Ph.D. thesis (2017).
78. Oriekhov, D. & Voronov, S. Current distribution and group velocities for electronic states on $\alpha - \mathscr{T}_3$ lattice ribbons in a magnetic field. *J. Phys. Condens. Matter* https://iopscience.iop.org/article/10.1088/1361-648X/abfd52 (2021).
79. Oriekhov, D., Gorbar, E. & Gusynin, V. Electronic states of pseudospin-1 fermions in dice lattice ribbon. *Low Temp. Phys.* **44**, 1313 (2018).
80. Bugaiko, O. & Oriekhov, D. Electronic states of pseudospin-1 fermions in lattice ribbons in a magnetic field. *J. Phys. Condens. Matter* **31**, 325501 (2019).
81. Cheng, X., Zhou, B., Zhou, B. & Zhou, G. Strain effect on electronic structure and transport properties of zigzag $\alpha - \mathscr{T}_3$ nanoribbons: A mean-field theoretical study. *J. Phys. Condens. Matter* **33**, 215301 (2021).
82. Raoux, A., Morigi, M., Fuchs, J.-N., Piéchon, F. & Montambaux, G. From dia-to paramagnetic orbital susceptibility of massless fermions. *Phys. Rev. Lett.* **112**, 026402 (2014).
83. Piéchon, F., Fuchs, J., Raoux, A. & Montambaux, G. Tunable orbital susceptibility in $\alpha - \mathscr{T}_3$ tight-binding models. *J. Phys. Conf. Ser.* **603**, 012001 (2015).
84. Soni, R., Kaushal, N., Okamoto, S. & Dagotto, E. Flat bands and ferrimagnetic order in electronically correlated dice-lattice ribbons. *Phys. Rev. B* **102**, 045105 (2020).
85. Tan, H., Xu, Y., Wang, J., Liu, J.-F. & Ma, Z. Valley filter and giant magnetoresistance in zigzag $\alpha - \mathscr{T}_3$ nanoribbons. *J. Phys. D Appl. Phys.* **54**, 105303 (2020).
86. Villegas, C. E., Tavares, M. R., Hai, G.-Q. & Vasilopoulos, P. Plasmon modes and screening in double metallic armchair graphene nanoribbons. *Phys. Rev. B* **88**, 165426 (2013).
87. Shylau, A., Badalyan, S., Peeters, F. & Jauho, A.-P. Electron polarization function and plasmons in metallic armchair graphene nanoribbons. *Phys. Rev. B* **91**, 205444 (2015).
88. Illes, E., Carbotte, J. & Nicol, E. Hall quantization and optical conductivity evolution with variable Berry phase in the $\alpha - \mathscr{T}_3$ model. *Phys. Rev. B* **92**, 245410 (2015b).
89. Brey, L. & Fertig, H. Elementary electronic excitations in graphene nanoribbons. *Phys. Rev. B* **75**, 125434 (2007).
90. Huang, D., Iurov, A., Xu, H.-Y., Lai, Y.-C. & Gumbs, G. Interplay of Lorentz-Berry forces in position-momentum spaces for valley-dependent impurity scattering in $\alpha - \mathscr{T}_3$ lattices. *Phys. Rev. B* **99**, 245412 (2019).
91. Ritchie, R. H. Plasma losses by fast electrons in thin films. *Phys. Rev.* **106**, 874 (1957).
92. Egerton, R. F. *Electron Energy-Loss Spectroscopy in the Electron Microscope* (Springer, 2011).
93. Horing, N., Tso, H. & Gumbs, G. Fast-particle energy loss in the vicinity of a two-dimensional plasma. *Phys. Rev. B* **36**, 1588 (1987).
94. Huang, D., Iurov, A., Gao, F., Gumbs, G. & Cardimona, D. Many-body theory of proton-generated point defects for losses of electron energy and photons in quantum wells. *Phys. Rev. Appl.* **9**, 024002 (2018).

Acknowledgements

Author contributions

A.I. and L.Z. conceived and originated this project. G.G. and D.H. substantially contributed to the development of the formalism and deriving the analytical equations. P.F., F.A., D.D. and N.W. performed numerical calculations and related computer programming. All authors reviewed the manuscript and contributed to its preparation.

Competing interests

The authors declare no competing interests.

Additional information

Supplementary Information The online version contains supplementary material available at https://doi.org/10.1038/s41598-021-99596-z.

Correspondence and requests for materials should be addressed to A.I.

Reprints and permissions information is available at www.nature.com/reprints.

Publisher's note Springer Nature remains neutral with regard to jurisdictional claims in published maps and institutional affiliations.